RSC Advances

PAPER

View Article Online
View Journal | View Issue

Cite this: *RSC Adv.*, 2025, **15**, 8300

Textile dye removal using diatomite nanocomposites: a metagenomic study in photosynthetic microalgae-assisted microbial fuel cells†

Anshuman Rai,[ab] Vandana Sirotiya,[c] Ankesh Ahirwar,[c] Gurpreet Singh,[c] Rajeev Kawatra,[b] Anil K. Sharma,[d] Harish[e] and Vandana Vinayak *[c]

In this study, Coomassie brilliant blue (CBB), brilliant green (BG), and rhodamine (Rh) dyes were used to simulate dye-rich wastewater. Adsorption and degradation of these dyes (2 μM, 10 μM, and 30 μM) on diatomite (DE) were evaluated under light (L) and dark (D) conditions. The adsorption of dye–DE composites followed pseudo-second-order kinetics at all concentrations and conditions had R^2 > 0.99, thus showing a good fit. The calculated equilibrium adsorption amount $q_{e,(cal)}$ was coherent with the value of experimental $q_{e,(exp)}$. The poorest adsorption and photocatalysis occurred at 30 μM, prompting the functionalization of dyes with TiO_2 and Fe_3O_4 nanoparticles (NP(s)). The highest dye degradation efficiencies (DG_{eff}) for 30 μM dyes were 86.79% (CBB–DE–Fe_3O_4, 72 h), 96.10% (BG–DE–TiO_2, 52 h), and 81.74% (Rh–DE–TiO_2, 48 h), with Rh–DE–TiO_2 showing the fastest degradation. Functionalized DE–dye (30 μM) nanocomposites were further tested in a photosynthetic microalgae-assisted microbial fuel cell with dye-simulated wastewater at the anode (PMA-MFC-1 with CBB–DE–Fe_3O_4, PMA-MFC-2 with BG–DE–TiO_2 and PMA-MFC-3 with Rh–DE–TiO_2) and *Asterarcys* sp. GA4 microalgae at the cathode. In dark anode chambers, PMA-MFC-3 achieved the highest DG_{eff} value of Rh dye as 88.23% and a polarization density of 30.06 mW m^{-2}, outperforming PMA-MFC-2 with BG dye and PMA-MFC-1 with CBB dye. The molecular identifier analysis of microbes in wastewater at the anode showed the dominance of Sphingobacteria and Proteobacteria in PMA-MFC-3 (Rh–DE–TiO_2) and COD removal of 61.36%, highlighting its potential for efficient dye degradation and bioelectricity generation. Furthermore, PMA-MFC-3 simultaneously demonstrated a superior microalgal lipid yield of 3.42 μg g^{-1} and an algal growth of 8.19 μg g^{-1} at the cathode.

Received 3rd February 2025
Accepted 3rd March 2025

DOI: 10.1039/d5ra00793c

rsc.li/rsc-advances

1 Introduction

Dyes from textile industries contribute to the largest amount of pollution to water resources, and they are one of the major health concerns.[1] India alone generates 38 354 million liters per day (MLD) of textile wastewater with a sewage treatment capacity of only 11 786 MLD.[2] Among the significant amount of colored wastewater generated, the major portion is from textile and tannery industries, which are rich in dyes and heavy metals. Besides causing water pollution, the colored substances of the dyes are resistant to biodegradation *via* conventional wastewater treatment strategies.[3] Based on the color index, there are 10 000 different dyes, which result in the production of ~700 000 tons of dye waste across the world, of which 1–15% are released into wastewaters during the dyeing process.[4] There are many structural varieties of dyes like acidic, basic, azo, metal complex and synthetic dyes.[5] These dyes are carcinogenic and cause respiratory, skin, and other health hazards.[6] While numerous physical and chemical methods exist for removing these dyes, they are often not cost-effective and lead to secondary chemical pollution, harming aquatic life and indirectly impacting the human health.[7,8] Numerous adsorbents and nanocomposites have gained attention for their photocatalytic properties, enabling the removal of dyes and colors through adsorption and degradation. The commonly used adsorbents are activated carbon, zeolites, and noble metals.[9]

Alternatively, treating such effluents with freely available diatomite is very economical.[10] DE, which is also known as diatomaceous earth, is formed from dead frustules of diatoms.[11]

[a]*MMU, Deemed University, School of Engineering, Department of Biotechnology, Ambala, Haryana, 133203, India*

[b]*Forensic Science Laboratory, Haryana, Madhuban, 132037, India*

[c]*Diatom Nanoengineering and Metabolism Laboratory, Dr Harisingh Gour Central University, School of Applied Science, Sagar, M.P, India, 470003. E-mail: kapilvinayak@gmail.com*

[d]*Department of Biotechnology, Amity School of Biological Sciences, Amity University Punjab, Mohali 140306, Punjab, India*

[e]*Department of Botany, Mohanlal Sukhadia University, Udaipur, Rajasthan, 313001, India*

† Electronic supplementary information (ESI) available. See DOI: https://doi.org/10.1039/d5ra00793c

Diatoms are unicellular microalgae rich in silica naturally present in all open water bodies.[12] They are natural reservoirs of organic silica, which varies from species to species.[13] Their walls are made up of a specific pattern of hole arrays, which are known as areola in their frustules.[14] The size of each pore in diatoms ranges from 1 to 100 nm.[15,16] The pores are further arranged in a nanopore array architecture, which is unique for each diatom species giving each diatom a different genus and species.[13] The nanoporous architecture increases the surface area, thus helping in removing heavy metals *via* different mechanisms such as biotransformation, biosorption, bioaccumulation and biomineralization.[17,18] They can adsorb heavy metals, pollutants, dyes and drugs on their surface, thus enhancing their removal to clean wastewater from industries.[10] A study demonstrated that amine-functionalized mesoporous diatom silica xerogels are efficient for the removal of Eriochrome black T (EBT) dye.[19] It was found that 100 mg of DE alone removed 50 mg L^{-1} dye by 58% and DE-modified xerogel by 99% in ~1 h.[19] Various metal organic frameworks can be easily functionalized on diatom's surface to form strong metal bound interactions on the surface of diatom frustules.[20] It can be a choice over expensive materials such as activated carbon for the adsorption, removal and degradation of textile dyed wastewater.[20] The present study involves the use of DE nanocomposites for the adsorption, removal, and degradation of three textile industrial dyes under light and dark conditions.

Another way of efficiently removing dyed wastewater is the use of microbial fuel cells (MFCs).[21] Microbial fuel cell techniques are efficient ways of removing dyes and other pollutants from various types of wastewater *via* a biochemical oxidation process.[22] Therefore, these dye–DE nanocomposites are utilized in a PMA-MFC to treat and degrade dyed wastewater while concurrently generating bioelectricity.[23,24] The use of live microalgae at the cathode in a PMA-MFC system offers the advantage of prolonged operation while ensuring a continuous supply of oxygen to the cathode.[25,26] In addition to safely sanitizing wastewater, microalgae can be used to produce value-added products such as its biomass, lipids, carotenoids, proteins, carbohydrates, biofuel, and bioplastics.[27,28] In the present study, oleaginous microalgae, cultured from the local water site, has been used at the cathode in PMA-MFCs projected to remediate dyed wastewater functionalised with DE nanocomposites at the anode. The dye–DE nanocomposites coated on the anode surface in the PMA-MFC not only facilitated nanocatalytic degradation but also underwent organic oxidation by anaerobic microbes in the anode chamber of PMA-MFC. The novelty of this study is that the metagenomic study of microbial community, their metabolism, role in the degradation of three different dyes using different sets of diatom nanocomposites in a PMA-MFC yielding algal biomass, value-added components, bioelectricity and remediated textile-dyed wastewater.

2 Material and methods

2.1 Adsorption of textile dyes on diatomite and nanoparticles

The DE and different industrial synthetic dyes, namely Coomassie brilliant blue (CBB), brilliant green (BG), and rhodamine (Rh), were purchased from HiMedia. Dye solutions with concentrations of 2 μM, 10 μM, and 30 μM for each of CBB, BG, and Rh were prepared, with their pH maintained at 7 using a phosphate buffer solution. These dyes were prepared at different concentrations in 5 mL of distilled water and used as controls in test tubes. The dye solutions were then mixed with 100 mg of diatomite (DE), which were washed with deionized water and dried at 100 °C, to create various test samples. The control and test samples were incubated at room temperature in light (0.45 lux) (L) and darkness (D) to observe their rate of adsorption and degradation using a UV-VIS spectrophotometer (LabIndia 3000) at different time intervals, 30 min till 1 h, and then at intervals of 24 h till 72 h.

The dye was first adsorbed onto DE and then exposed to light (a physical catalyst) or nanoparticles (a chemical catalyst) to measure how efficiently the dyes were degraded. The dye–DE combinations with the lowest dye DG_{eff} were further treated with NP(s) to see if they improved, slowed down, or had no effect on the dye removal or degradation rate. The NP(s) used in this study were titanium dioxide (TiO_2) and magnetite (Fe_3O_4) purchased from Sigma. These NP(s) were doped on DE *via* simple incubation in UV light and tested at a very low concentration of 0.2 μg mL^{-1} to be economic and environment-friendly.[29] Both the TiO_2–DE and Fe_3O_4–DE nanocomposites were checked for their nano photocatalytic degradation of the above-mentioned three dyes. TiO_2 is photocatalytic[30] and environment-friendly with a strong oxidative potential, and hence, it is popularly used for the degradation of pollutants in wastewater.[31] The magnetite (Fe_3O_4) NP(s) have electromagnetic properties, chemical stability and biocompatibility to remove heavy metals and organic pollutants from wastewater.[32] These NP(s) can generate reactive oxygen species (ROS) such as hydroxyl radicals ($^{\bullet}OH$) and superoxide anions ($O_2^{\bullet -}$), which degrade dye molecules into smaller, non-toxic compounds.[33]

The amount of dye adsorbed (q_e) onto the adsorbent at time (t), which is the amount of dye adsorbed by DE (g) measured in mg g^{-1}, is presented as eqn (1):

$$q_t = \frac{(C_0 - C_t)V}{m} \quad (1)$$

where C_0 is the initial concentration (mg L^{-1}), C_t is the concentration at time t (min), V is the volume of solution (L), and M is the mass of adsorbent (g). The pseudo-second-order kinetics was calculated using eqn (2):

$$\frac{1}{q_t} = \frac{1}{k_2 q_e^2} + \frac{t}{q_e} \quad (2)$$

where q_e is the equilibrium adsorption capacity (mg g^{-1}) at equilibrium, k_2 is the rate constant for pseudo-second-order adsorption (g mg^{-1} min^{-1}) and q_t is the adsorption capacity at time t (mg g^{-1}).

Using the calculated q_t, plot the data $1/q_t$ *versus* t to determine the value of q_e and k_2.

The DG_{eff} of dyes at various compositions and concentrations was calculated using eqn (3):

$$DG_{eff} = \frac{C_0 - C_t}{C_0} \times 100 \quad (3)$$

where C_0 is the initial concentration and C_t is the final concentration.

2.2 Photosynthetic microalgae-assisted microbial fuel cells for the remediation of dyes and electricity generation

The three dyes (CBB, BG, and Rh) were tested at concentrations of 2 μM, 10 μM, and 30 μM in combination with DE and NP in test tubes, under both light and dark conditions. The nanocomposite concentrations exhibiting poor DG_{eff} in the test tubes were subsequently evaluated in a PMA-MFC setup for further degradation. Accordingly, three distinct PMA-MFC configurations were designed, each corresponding to the nanocomposites with one of the three dyes. Three microbial fuel cells were thus constructed with a ceramic plate acting as proton exchange membrane as per the protocol suggested by Das *et al.*, 2020 [34] with modification of living microalgae at the cathode and thus known as PMA-MFCs. These three PMA-MFCs contained CBB, BG, and Rh dyes individually, along with DE and NP(s) (TiO_2 and Fe_3O_4) at the anode and were thus labeled as PMA-MFC-1, PMA-MFC-2, and PMA-MFC-3, respectively. The dyes in all the three PMA-MFCs were mixed with synthetic wastewater (SWW) (recipe ESI Table 1,†[35]) and activated sludge at anode chamber. The wastewater sludge was collected from Green hostel at Dr Harisingh Gour Vishwavidyalaya (A Central university), Sagar, M.P, India. The cathode and anodes were made of graphite felt purchased from Marine lines, Mumbai. The cell potential of PMA-MFC reactors 1, 2 and 3 were tested for resistance ranging from 20 000 Ω to 5 Ω using a resistance box (Model Bexco, total resistance 21 110 Ω, manganin coil, 9/16″, thick brass blocks, resistance in ohms: 1–10000 Ω). The anode chamber contained SWW as the anolyte of volume ~400 mL simulated with the dye of concentration, which showed least DG_{eff} in a test tube (L/D). The graphite felt at the anode was 11 cm in length and 3 cm in breadth. It was further coated with DE–NP (Fe_3O_4/TiO_2) depending upon which DE and NP combination showed the best DG_{eff} for the respective dyes as in the case of WO_3 as a novel catalyst in an MFC.[36] The doping of Fe_3O_4 and TiO_2 with DE on the graphite felt at the anode of PMA-MFCs was checked using a scanning electron microscope (SEM; Model NOVA NANO SEM 450 FEI CO. OF USA (S.E.A.) PTE LTD, SINGAPORE). Fe_3O_4 and TiO_2 NP elemental analysis was performed by SEM-EDX. The cathode was further filled with green microalgae collected from a water site in Sagar, Madhya Pradesh, India (24°45′46″N 78°14′02″E) and identified *via* Molecular Identifier (MID) Analysis.[37] Then about 69×10^6 mL/400 mL microalgal cells were inoculated in classical BG-11 media,[38] which acted as the catholyte at the cathode and was exposed to light (0.72 Klux) for a photoperiod of 12 h light : 8 h darkness in PMA-MFCs 1 to 3. Here we compared the three PMA-MFCs with different dye nanocomposites at the anode, hence the control PMA-MFC without dye nanocomposite was not used.

2.2.1 Chemical oxygen demand. The chemical oxygen demand (COD) of synthetic wastewater (SWW)-simulated dyed water at the anode was estimated on the initial and final days of the PMA-MFC reactor for the average period of 30 days in all three PMA-MFC reactors. The polarization curve and coulombic efficiency were calculated for each MFC reactor as per standard calculations[39] following eqn (4) and (5):

$$P = V \times I \tag{4}$$

where V is the voltage (V) and I is the current in (A).

The coulombic efficiency (CE) was calculated using eqn (5):

$$\mathrm{CE} = \frac{M \int_0^t I\,\mathrm{d}t}{FbV\Delta\mathrm{COD}} \tag{5}$$

where M is the molecular weight of oxygen, I is the current (A), t is the time (s), F is the Faraday constant, b is the required numbers of electrons for the reduction of 1 mol oxygen, V is the volume of the anode chamber, and ΔCOD is the change in COD over time t.

2.2.2 Normalized energy recovery. The normalized energy recovery (NER) data representing the energy in MFCs[40] was also calculated for all PMA-MFCs simulated to remediate CBB, BG and Rh dyes, as shown in eqn (6):

$$\mathrm{NER} = \frac{(\mathrm{Power})}{(\text{Wastewater flow rate}) \times (\Delta\mathrm{COD})} \tag{6}$$

2.3 Identification of microorganisms at the anode and cathode

2.3.1 The 16S–V3V4 metagenomics sequencing: library preparation. The maximum power density or, in other terms, the efficiency of an MFC depends upon the rate of oxidation by microbes at the anode for the production of bioelectricity.[41] The efficiency of degradation of wastewater is highly dependent upon the type of electrogenic microbe, which acts as a biocatalyst to oxidize organic matter and transfer electrons *via* substrate oxidation.[42] Therefore, to identify the population of such microbes dominating in the wastewater at the anode, their population density was analyzed *via* metagenomics.[43] DNA extraction of microbes in wastewater was performed for PMA-MFC 1–3 rich in CBB, BG and Rh dyes using a Qiagen biostic bacteraemia kit, Germany (catalogue number: 12 240–50).[44] All samples were quantified using a Qubit DNA HS Assay (Invitrogen, Cat#Q32854). The DNA sample was diluted to 5 ng (For "Too Low" sample, 5 μL DNA was taken for PCR) and was amplified for the 16s region (1500 bp) followed by V3V4 (460 bp) using 16s and V3V4 primers, respectively, in a nested PCR approach. Positive and no template controls were included in the PCR. These PCR products were checked on agarose gel. All amplified PCR products were then cleaned up (1X) using AMPure XP beads (Beckman Coulter, Cat#A63882) to get rid of non-specific fragments before proceeding with library preparations. The PCR products were further taken for DNA library preparation using a NEB Next Ultra DNA Library Prep Kit for Illumina (NEB, Cat# E7370L). The amplicons were end repaired and mono-adenylated at 3′ end in a single enzymatic reaction. NEB hairpin-loop adapters are ligated to the DNA fragments in a T4-DNA ligase-based reaction. Following ligation, the loop containing Uracil is linearized using a USER Enzyme (a combination of UDG and Endo VIII), to make it available as

a substrate for PCR-based indexing in the next step. During PCR, barcodes were incorporated using unique primers for each of the samples, thereby enabling multiplexing. All prepared libraries were checked for fragment distribution using a 5300 fragment analyser system (Agilent). Prepared libraries were quantified using a Qubit HS Assay (Invitrogen, Cat# Q32854). The obtained libraries were pooled and diluted to a final optimal loading concentration using a MiSeq instrument (2 × 250 cycles, Cat# MS1022003). The generated sequence data were assessed for quality control and processed to generate FASTQ files. The primer details used were 16SF 5′ AGAGTTTGATCCTGGCTCAG'3, 16SR 5'GGTTACCTTGTTACGACTT'3, V3V4F 5'CCTACGGGNGGCWGCAG'3 and V3V4R 5'GACTACHVGGGTATCTAATCC'3.[45]

2.3.2 Molecular identifier (MID) analysis for identifying microalgae at the cathode. The quality of DNA from the unknown microalga to be used in PMA-MFC was evaluated prior on 1.0% agarose gel. A single band of high-molecular-weight DNA was observed. A fragment of *18S rDNA* gene was amplified by 32F and 634R primers. A single discrete PCR amplicon band of 1500 bp was observed when resolved on Agarose gel. The PCR amplicon was purified to remove contaminants. Forward and reverse DNA sequencing reactions of PCR amplicon were carried out with forward primer and reverse primers using a BDT v3.1 Cycle sequencing kit on an ABI 3730xl Genetic Analyzer. A consensus sequence of 18S rDNA gene was generated from forward and reverse sequence data using the aligner software. The 18S rDNA gene sequence was used to carry out BLAST with the NCBI gene bank database. Based on the maximum identity score, the first ten sequences were selected and aligned using the multiple alignment software program Clustal W.[46] The distance matrix was generated and the phylogenetic tree was constructed using the MEGA X. Data.[47]

2.3.3 Biochemical analysis of microalgae at the cathode. Microalgal cell growth and optical density were recorded using a UV-VIS spectrophotometer (Model: LabIndia 3000) at 735 nm for a period of 33 days for each PMA-MFC. The cell biomass was evaluated as dry weight yield using eqn (7):

$$\text{Total weight of biomass} = \text{weight of tube with sample} - \text{weight of empty tube} \quad (7)$$

The lipid yield was measured following the sulfo-phospho-vanillin method[48] using linseed oil as the standard purchased from Sigma.

3 Results and discussion

3.1 Dyes adsorption

The dye adsorption kinetics was estimated for CBB, BG and Rh dyes on DE. The pseudo-second-order kinetics of dye adsorption, showing t/q_t *versus* time, is represented in Fig. 1. The two curves in one plot of Fig. 1 correspond to the adsorption of dye under light (L) and dark (D) conditions at different

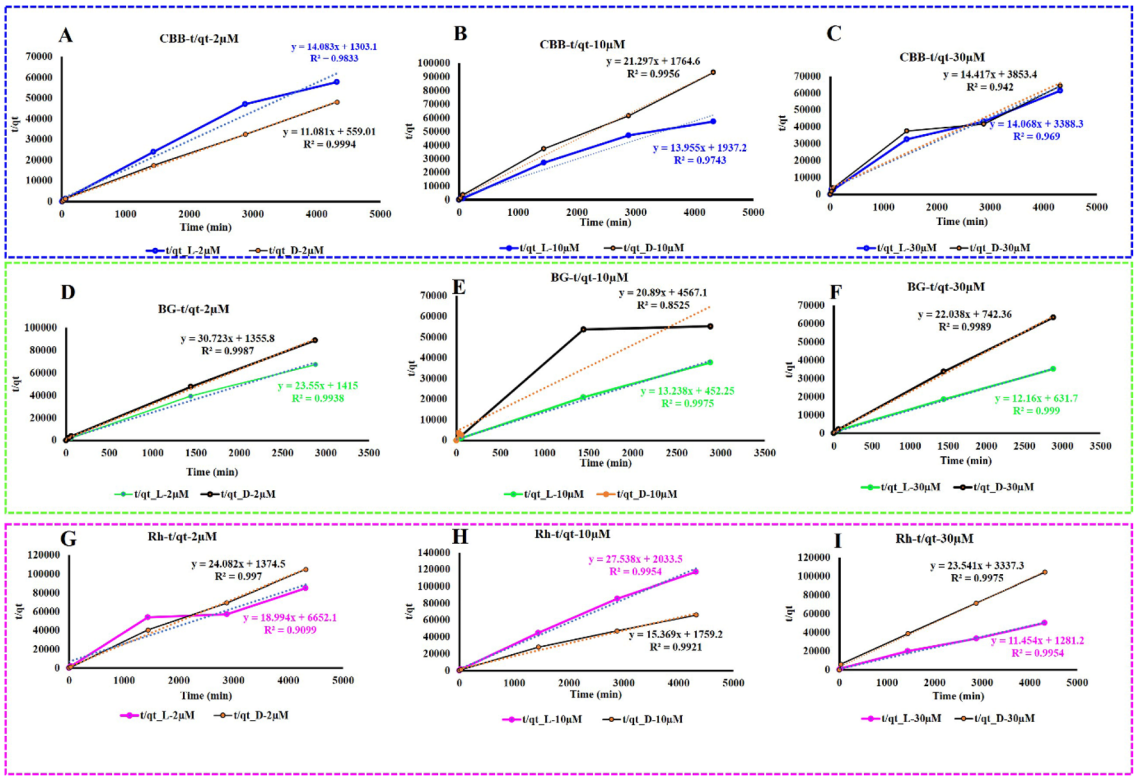

Fig. 1 Pseudo-second-order kinetics for dyes: (A) CBB 2 μM, light and dark conditions; (B) CBB 10 μM, light and dark conditions; (C) CBB 30 μM, light and dark conditions; (D) BG 2 μM, light and dark conditions; (E) BG 10 μM, light and dark conditions; (F) BG 30 μM, light and dark conditions; (G) Rh 2 μM, light and dark conditions; (H) Rh 10 μM, light and dark conditions; and (I) Rh 30 μM, light and dark conditions.

concentrations (2 μM, 10 μM and 30 μM). The $q_{e,(cal)}$ and $q_{e,(exp)}$ show a perfect correlation, as shown in Fig. 1. The linear regression (R^2) in this pseudo-second-order kinetics is more than 0.99 in all plots (Fig. 1A to I), showing a good straight-line slope for the adsorption of all dyes in all concentrations onto DE. The lower concentration dyes at 2 μM showed almost same $q_{e,(cal)}$ and $q_{e,(exp)}$ for all dyes, which were ~0.07 mg g^{-1} in L and 0.09 mg g^{-1} in D for CBB, ~0.04 in L and 0.03 mg g^{-1} in D for BG, and ~0.05 mg g^{-1} in L and 0.04 mg g^{-1} in D for Rh. However, the $q_{e,(cal)}$ and $q_{e,(exp)}$ under light conditions were slightly higher for all the three dyes compared to that under dark conditions at higher concentrations, *i.e.* at 10 μM (~0.07 mg g^{-1} in L and 0.04 mg g^{-1} in D for CBB, ~0.07 mg g^{-1} in L and 0.05 mg g^{-1} in D for BG, and ~0.08 mg g^{-1} in L and 0.04 mg g^{-1} in D for Rh). The dyes at 30 μM of dye concentration followed the same pattern under light and dark conditions, and the $q_{e,(cal)}$ and $q_{e,(exp)}$ values were almost similar with no significant change. The kinetic constant k_2, $q_{e,(cal)}$ and $q_{e,(exp)}$ and R^2 for all dyes are shown in ESI Fig. S1.† Hence, in comparison, the pseudo-second-order kinetics represents and fits the adsorption kinetics data of CBB, BG and Rh dyes on DE. A study on the adsorption of malachite green on tamarind seeds also followed the linear regression plots, where $q_{e,(cal)}$ and $q_{e,(exp)}$ values were coherent and the R^2 values were above 0.98.[49] Similarly, the adsorption of methylene blue dye on a zinc-derived (ZD) porous nanosystem showed the pseudo-second-order rate model (rate constant = 0.00011 g mg^{-1} min^{-1}; adsorption capacity ($q_{e,(cal)}$) = 386.1 mg g^{-1}; R^2 = 0.990)[50]

3.2 Dyes degradation

3.2.1 Degradation of Coomassie brilliant blue (CBB) dye. The control sample with only CBB dye (2 μM, 10 μM and 30 μM), *i.e.* devoid of DE, showed an absorption spectrum at 555 nm and its DG_{eff} was observed under light and dark conditions at different time periods. The initial concentration of 2 μM, 10 μM, and 30 μM CBB in light was 180.45 μg mL^{-1}, 257.65 μg mL^{-1}, and 317.14 μg mL^{-1} which declined to 50.64 μg mL^{-1}, 146.52 μg mL^{-1}, and 196.68 μg mL^{-1} in 72 h (Fig. 2A). On the other hand, the initial concentration of 2 μM, 10 μM, and 30 μM CBB under dark conditions was 239.94 μg mL^{-1}, 306.32 μg mL^{-1}, and 385.98 μg mL^{-1}, which declined to 163.24 μg mL^{-1}, 211.43 μg mL^{-1} and 300.92 μg mL^{-1} in 72 h in the analyzed supernatant (Fig. 2B). Control CBB dye in light showed dye DG_{eff} for 2 μM, 10 μM and 30 μM CBB as 71.93%, 43.12% and 37.98%, respectively, and in darkness as 31.96%, 30.97% and 22.03%, respectively (Fig. 2C). This certainly shows that CBB dye DG_{eff} is dependent not only on the light/dark conditions but also on the strength of the dye concentrations. It is because dye molecules under light exposure adsorb photons with an energy which is greater than their bandgap leading to the excitation of valence electrons. This produces unstable excited dye radicals, which lead to their degradation.[51] The difference in DG_{eff} of light and darkness in 2 μM CBB is greater (39.17%) than the DG_{eff} value of light and darkness in 30 μM CBB (15.95%), showing that a higher concentration of dye (30 μM CBB) shows no effect on its degradation under light and dark conditions. This is because at higher concentrations, dye molecules themselves block further light reaching deeper in the solution (shading effect), reducing their photocatalysis or photodegradation.[52] Further when diatomite was used as the adsorbent and exposed to light, the CBB–DE composite adsorbed as well went photocatalytic degradation. Upon exposure to light, CBB–DE (2 μM) showed its concentration decreasing from 0 min to 72 h at a smooth fall from its initial concentration of 40.41 μg mL^{-1} at 0 min to 10.40 μg mL^{-1} in 24 h and further reaching 3.0 μg mL^{-1} in 72 h (Fig. 2D), thus showing 92.33% DG_{eff} in 72 h for CBB (2 μM)–DE. For CBB (10 μM)–DE, the adsorption rate increased, showing the dye concentration in supernatant falling from 45.91 μg mL^{-1} at 0 min to 19.58 μg mL^{-1} in 24 h. In CBB (30 μM)–DE, the concentration decreased from 50.38 μg mL^{-1} at 0 min to 28.35 μg mL^{-1} in 24 h. The rate of dye degradation followed the same pattern in darkness except that the rate of adsorption was poor, and hence, the dye concentration in the supernatant was reduced from 66.40 μg mL^{-1} to 21.52 μg mL^{-1} for 2 μM, 56.42 μg mL^{-1} to 33.24 μg mL^{-1} for 10 μM, 67.70 μg mL^{-1} to 34.13 μg mL^{-1} for 30 μM CBB in 72 h (Fig. 2E). The DG_{eff} values at 2 μM, 10 μM and 30 μM of the CBB dye in DE under light conditions were observed to be 92.33%, 82.22% and 69.61%, respectively (Fig. 2F). However, the DG_{eff} values at 2 μM, 10 μM and 30 μM of the CBB dye in DE under dark conditions were found to be 67.58%, 41.07% and 49.58%, respectively. This may be essentially due to less adsorption and degradation of dyes under dark conditions.[53] In a study, polyphenylene diamine-grafted electrospun carbon nanofibers were used to remove the toxic dye CBB *via* a charge–discharge process strengthening the electrostatic interactions between the polymer and the dye.[54] In contrast, studies have demonstrated the use of diatomite as an effective adsorbent on an industrial scale for treating methylene blue and acid orange dye-rich wastewater.[55] In this study, magnesium oxide-modified diatomite waste (MgO-DW) was used to remove organic dyes depending upon its exposure time, initial concentration of dyes and pH when exposed to the MgO-DW surface for different time periods.[55] The diatomite and dye concentrations were characterized by FTIR spectra and adsorption isotherm analysis, proving that MgO-DW is an excellent adsorbent for cationic and anionic dyes.

3.2.1.1 Coomassie brilliant blue nanocomposites. Since CBB at a concentration of 30 μM showed the least DG_{eff}, even under light conditions, the 30 μM CBB–DE mixture was thus functionalised with TiO_2 and Fe_3O_4 NP(s). The NP(s) were added at a minimal concentration of 0.2 μg mL^{-1} to assess whether there was any enhancement in degradation through nano catalytic activity. The CBB–DE–Fe_3O_4 nanocomposites facilitated nano photocatalytic degradation of dyes with the remaining amount of dyes in supernatant reduced to 5.35 μg mL^{-1} from its initial concentration of 39.37 μg mL^{-1} in 24 h (Fig. 2G). On the offset with CBB–DE–TiO_2 nanocomposites, the dye showed a remaining concentration of 15.39 μg mL^{-1} in the supernatant at 24 h from its initial concentration of 31.81 μg mL^{-1} (Fig. 2G). This is better than CBB (30 μM) degradation without Fe_3O_4/TiO_2 NP(s), where the initial concentration dropped from 50.38 μg mL^{-1} to 28.35 μg mL^{-1} in 24 h and to 15.3 μg mL^{-1} in 72 h upon exposure to light (Fig. 2D). The TiO_2 NP-doped CBB–DE in light

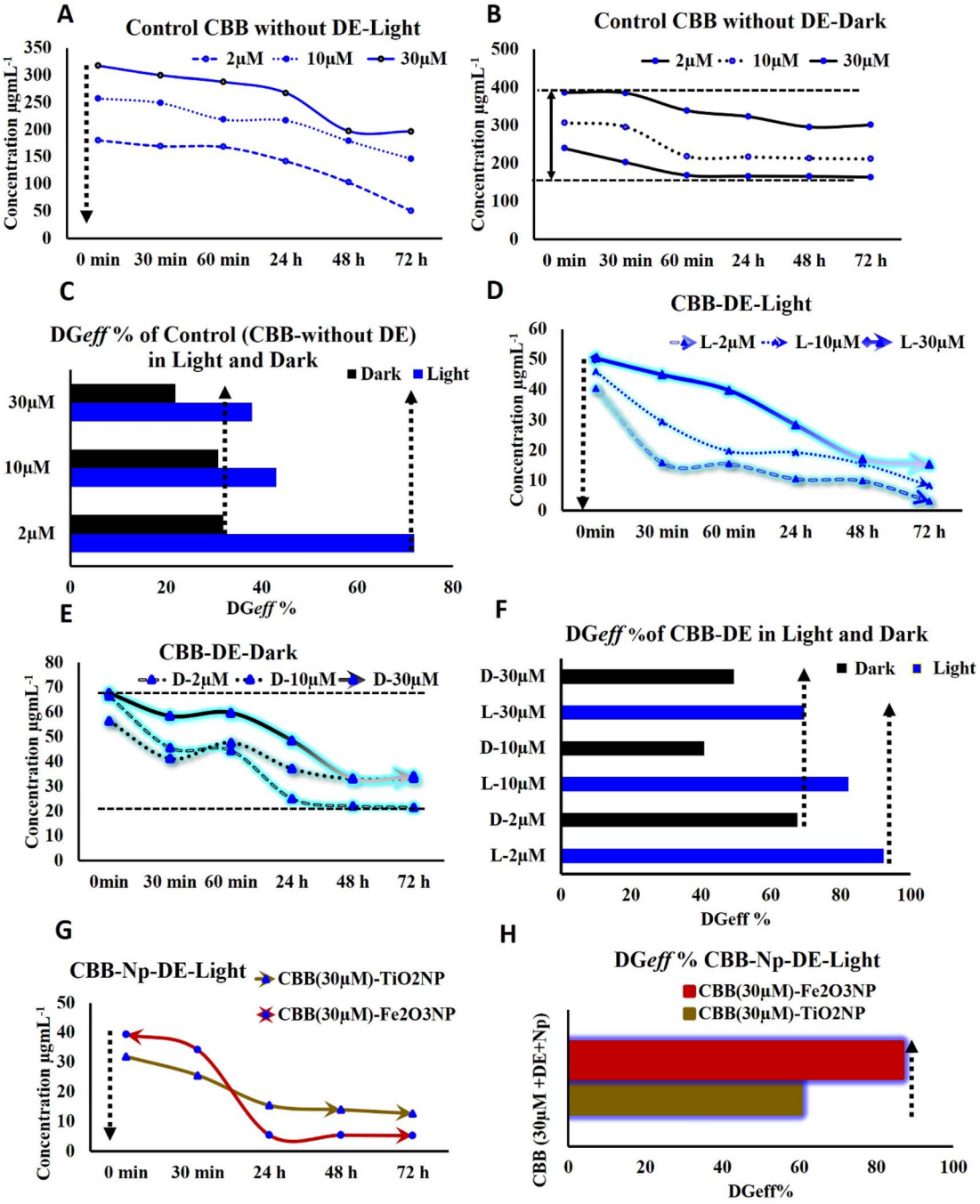

Fig. 2 Time-dependent (A) concentration of the control CBB sample without DE under light condition; (B) control CBB sample without DE under dark condition; (C) DG_{eff} of control CBB without DE under light and dark conditions; (D) CBB with DE under light condition; (E) concentration of CBB with DE under dark condition; (F) DG_{eff} of CBB and DE under light and dark conditions; (G) concentration of CBB (30 μM) with DE and nanoparticles (TiO_2 and Fe_3O_4) and (H) DG_{eff} of the highest CBB dye concentration in the presence of nanoparticles (TiO_2 and Fe_3O_4).

showed a DG_{eff} value of 60.27% and 86.79% with Fe_3O_4 in 72 h and 69.61% without NP(s) in 72 h, showing that TiO_2 did not improve CBB degradation and was poor in performance compared to Fe_3O_4 (Fig. 2H). Other studies have shown the use of chitin nanoparticles for the effective removal of a fixed concentration of CBB, methylene blue and bromophenol blue dyes.[56] They also showed that the increasing dye concentration has decreased the rate of adsorption and increasing chitin NP(s) content increased the adsorption of dyes.[56] Similarly, the thiourea-modified Fe_3O_4/graphene oxide nanocomposite showed 86% efficient removal of CBB from aqueous solutions.[57]

3.2.2 Brilliant green (BG) dye. The DE also exhibited a remarkable adsorption capacity for different concentrations of BG at 550 nm. The control having only BG dye at 2 μM, 10 μM and 30 μM without DE under light and darkness showed dye degradations, as shown in Fig. 3A–C. Under light conditions, BG

dye at 2 μM, 10 μM and 30 μM without DE showed initial concentrations (0 min) of 25.78 μg mL^{-1}, 58.10 μg mL^{-1} and 103.68 μg mL^{-1} which decreased to 13.93 μg mL^{-1}, 18.51 μg mL^{-1} and 64.23 μg mL^{-1} in the supernatant, respectively, in 48 h (Fig. 3A). The BG degradation without DE in darkness, however, showed poor degradation (Fig. 3B). The concentration of control BG at 2 μM, 10 μM and 30 μM in the supernatant initially at 0 min was 249.29 μg mL^{-1}, 317.63 μg mL^{-1}, and 391.88 μg mL^{-1}, respectively, which decreased to 175.53 μg mL^{-1}, 238.47 μg mL^{-1}, and 321.08 μg mL^{-1} at 48 h, respectively, under dark conditions. The DG_{eff} value for control BG 2 μM, 10 μM and 30 μM under light was 45.95%, 68.13% and 38.05%, respectively, and 29.58%, 24.92% and 18.06%, respectively, in darkness, showing that the DG_{eff} value is poor for the BG dye at all its tested concentrations in darkness (Fig. 3C). Fig. 3D shows BG 2 μM, 10 μM and 30 μM concentration with DE in light at 0 min as 25.18 μg mL^{-1}, 58.47 μg mL^{-1} and 99.44 μg mL^{-1}, respectively, which dropped to 3.77 μg mL^{-1}, 10.43 μg mL^{-1} and 58.71 μg mL^{-1}, respectively, in 48 h. Under dark conditions, BG with 2 μM, 10 μM and 30 μM with DE showed initial concentrations of 22.68 μg mL^{-1}, 48.47 μg mL^{-1}, and 99.43 μg mL^{-1}, which declined to 6.46, 22.41 and 76.74 in 48 h (Fig. 3D). It was found that the BG dye at 2 μM, 10 μM and 30 μM concentrations in the BG-DE mixture upon exposure to light showed DG_{eff} values of 85.03%, 78.47% and 40.96% in light (Fig. 3E), and only 58.80%, 53.75% and 22.82% in darkness (Fig. 3F). This showed

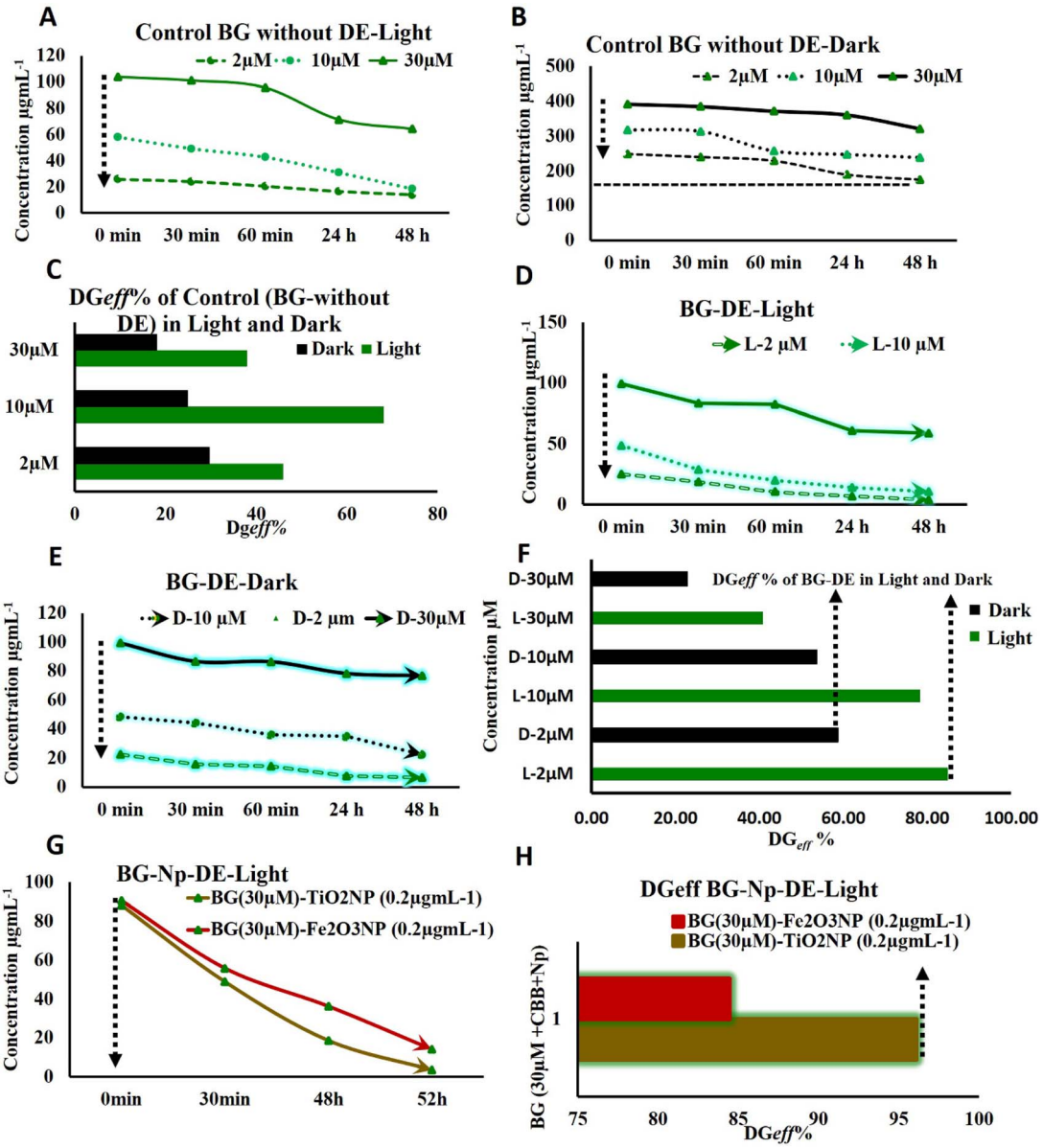

Fig. 3 Time-dependent (A) concentration of the control BG sample without DE under light condition; (B) control BG sample without DE under dark condition; (C) DG_{eff} of control BG without DE under light and dark conditions; (D) BG with DE under light condition; (E) concentration of BG with DE under dark condition; (F) DG_{eff} of BG and DE under light and dark conditions; (G) concentration of BG (30 μM) with DE and nanoparticles (TiO_2 and Fe_3O_4) and (H) DG_{eff} of the highest BG dye concentration in the presence of nanoparticles (TiO_2 and Fe_3O_4).

that except 2 μM and 10 μM BG–DE, 30 μM BG–DE dye mixture was completely saturated in 24 h, as all the porous surfaces in DE were covered by the dye, resulting in poor adsorption rates after 24 h and hence lower rate of photocatalytic dye degradation. The removal of BG has been studied with various adsorbents such as kaolin,[58] rice husk ash,[59] bagasse fly ash,[60] activated carbon,[61] tea powder,[62] red clay,[63] areca nut husk,[64] *Bambusa tulda*,[65] and jute sticks.[66] The adsorption of BG on rice husk ash is effectively increased with the increase in temperature.[59] Similarly, the biocomposites of chitosan/functionalized fruit stones are effective in the removal of BG with an electrostatic adsorption capacity of 409.63 mg g^{-1}.[67] The results and efficacy of the removal of dye depend upon many factors such as type of dye and its pH dependence, amount of dye to be removed, amount of DE, surface modification, light and dark conditions, surface modifications, and time.

3.2.2.1 Evaluating brilliant green nanocomposites. To enhance the adsorption and degradation of BG dye on DE, nanoparticles, TiO_2 and Fe_3O_4 NP(s) (0.2 μg mL^{-1}) were added individually to the BG dye at 30 μM concentration because it showed the poorest DG_{eff} (40.96% in light, since light outperformed degradation than dark conditions). The BG dye–DE–TiO_2 nanocomposite showed 88.18 μg mL^{-1} dye at 0 min and 3.43 μg mL^{-1} dye left in supernatant in 52 h (Fig. 3G). Furthermore, the BG dye–DE–Fe_3O_4 nanocomposite dye content decreased from 90.65 μg mL^{-1} to 14.08 μg mL^{-1} in 52 h (Fig. 3G).

Among the two NP(s) used, TiO_2 showed enhanced degradation of the BG (30 μM)–DE complex with a DG_{eff} value of 96.10% and Fe_3O_4 showed degradation of BG (30 μM)–DE with a DG_{eff} value of 84.45% in 48 h (Fig. 3H). In comparison to the DG_{eff} value of 40.96% in BG dye–DE without NP(s) exposed to light in 48 h (Fig. 3E), NP(s) definitely increased DG_{eff}. In a recent study, copper sulfide nanoparticles helped in 99% photocatalytic degradation of BG dye using 5 g L^{-1} of the nanoparticles in 20 min.[68] The quantity of NP(s) used in this study is, however, far less, about 200 μg L^{-1}, and further, this quantity of NP(s) was tested on the highest concentration of dye (30 μM). Therefore, the estimated time of degradation is longer in the present study compared to Andrew *et al.*'s (2024) study (20 min).[68] A study has shown that CaO nanospheres from egg shells have better adsorption properties for BG (98%) compared to phenol red (78%).[69] This shows that the adsorbent material is selective for dye removal, and in the present case, diatomite had nanopores and developed multiple adsorption sites and stability with strong van der Waals, hydrogen bonds, electrostatic and π–π stacking force with ionic dye molecules.[70]

3.2.3 Rhodamine dye (Rh) dye. The Control Rh without DE exposed to light at 2 μM, 10 μM and 30 μM at 0 min was 26.55 μg mL^{-1}, 52.12 μg mL^{-1} and 115.05 μg mL^{-1} falling to 9.19 μg mL^{-1}, 13.52 μg mL^{-1}, and 30.63 μg mL^{-1} in 72 h (Fig. 4A–C). In contrast, under dark conditions, the Rh initial amount at 2 μM, 10 μM and 30 μM were 45.23 μg mL^{-1}, 89.98 μg mL^{-1} and 166.68 μg mL^{-1}, which were only 10.32 μg mL^{-1}, 27.53 μg mL^{-1} and 52.12 μg mL^{-1} in 72 h. The DG_{eff} value of control Rh in light was 65.37%, 74.06% and 73.38%, and in darkness, it was 77.17%, 69.40% and 68.73% for 2 μM, 10 μM and 30 μM Rh dye, as shown in Fig. 4A–C, which is better than DG_{eff} of CBB and BG which was only 18–71% (Fig. 2A–C & 3A–C). However, Rh of 2 μM, 10 μM and 30 μM in the presence of DE under light conditions shows dye quantity falling from its initial amount of 33.32 μg mL^{-1}, 32.56 μg mL^{-1}, and 82.94 μg mL^{-1} to 7.88 μg mL^{-1}, 14.12 μg mL^{-1}, and 40.19 μg mL^{-1} in the supernatant, respectively, in the three different concentrations of Rh (Fig. 4D). On the offset, under dark conditions, Rh (2 μM, 10 μM and 30 μM) with DE showed its initial quantity of 50.62 μg mL^{-1}, 84.46 μg mL^{-1}, and 98.07 μg mL^{-1} declining to 30.02 μg mL^{-1}, 51.77 μg mL^{-1}, and 77.34 μg mL^{-1} in 72 h (Fig. 4E). The DG_{eff} values of Rh at 2 μM, 10 μM and 30 μM with DE were thus 76.33%, 56.64%, and 51.53% in light compared to that in darkness as 40.70%, 38.70%, 21.14% (Fig. 4F). Earlier studies have shown how DE modified with an EDA-TMC polymer acts as an effective adsorbent with an adsorbent capacity of 371.6 mg g^{-1} at pH 6.[71] Therefore, similar to CBB and BG, Rh, whose concentration was high (30 μM), showed the poorest DG_{eff} value and were thus functionalised with NP(s) for improving its adsorption and removal properties.

3.2.3.1 Evaluating rhodamine nanocomposites. When 30 μM of Rh–DE was functionalised with 0.2 g mL^{-1} of TiO_2 NP(s) and Fe_3O_4 NP(s) individually, the DG_{eff} value with TiO_2 NP(s) was better (81.74%) than that of Fe_3O_4 NP(s) (75.19%) in 52 h. The TiO_2 NP(s) catalyzed the adsorption of Rh on the surface of DE with the dye concentration in the supernatant falling from 32.33 μg mL^{-1} initially at 0 min to 5.90 μg mL^{-1} in 52 h (Fig. 4G). However, with the Fe_3O_4 NP(s) as a catalyst functionalized on the Rh–DE mixture, the initial concentration of the Rh dye was 49.23 μg mL^{-1} in 0 min and was left to 12.21 μg mL^{-1} in 52 h (Fig. 4H). This was much better than the DG_{eff} value of 49.11% with only Rh–DE without NP(s) in 72 h. This study is concordant with previous studies where TiO_2 diatomite has been used to remove Rh dye.[72]

3.3 Application: photosynthetic microalgae-assisted microbial fuel cells

The three different dyes CBB, BG and Rh were simulated to make dye-rich synthetic wastewater and used for testing *in situ* removal *via* electrochemical oxidation. This involved the setup of photosynthetic microalgae-assisted microbial fuel cells (PMA-MFCs) along with graphite electrodes. The dye–DE–NP(s) composite was brushed on anode graphite surface and dried. The graphite anode had dye-simulated SWW as electrolytes at the anode and microalgal cells as catholytes at the cathode.

3.3.1 Characterisation of the felt at the anode and cathode in a PMA-MFC. The graphite felt at the anode was characterised by SEM; ESI Fig. S2A† shows the diatomite and Fe_3O_4 nanocomposite at a scale bar of 500 nm, and ESI Fig. S2B–D† show different graphite felts and DE–Fe_3O_4 at scale bars of 40 μm, 3 μm and 10 μm. Similarly, ESI Fig. S3A† shows diatomite and TiO_2 at a scale bar of 500 nm and ESI Fig. S3B–D† show the graphite felt functionalised with DE–TiO_2 nanocomposites at scale bars of 200 μm and 30 μm seen from different positions. This showed that the dye–DE–NP(s) nanocomposites had well been functionalised on the fibres of the graphite felt. The

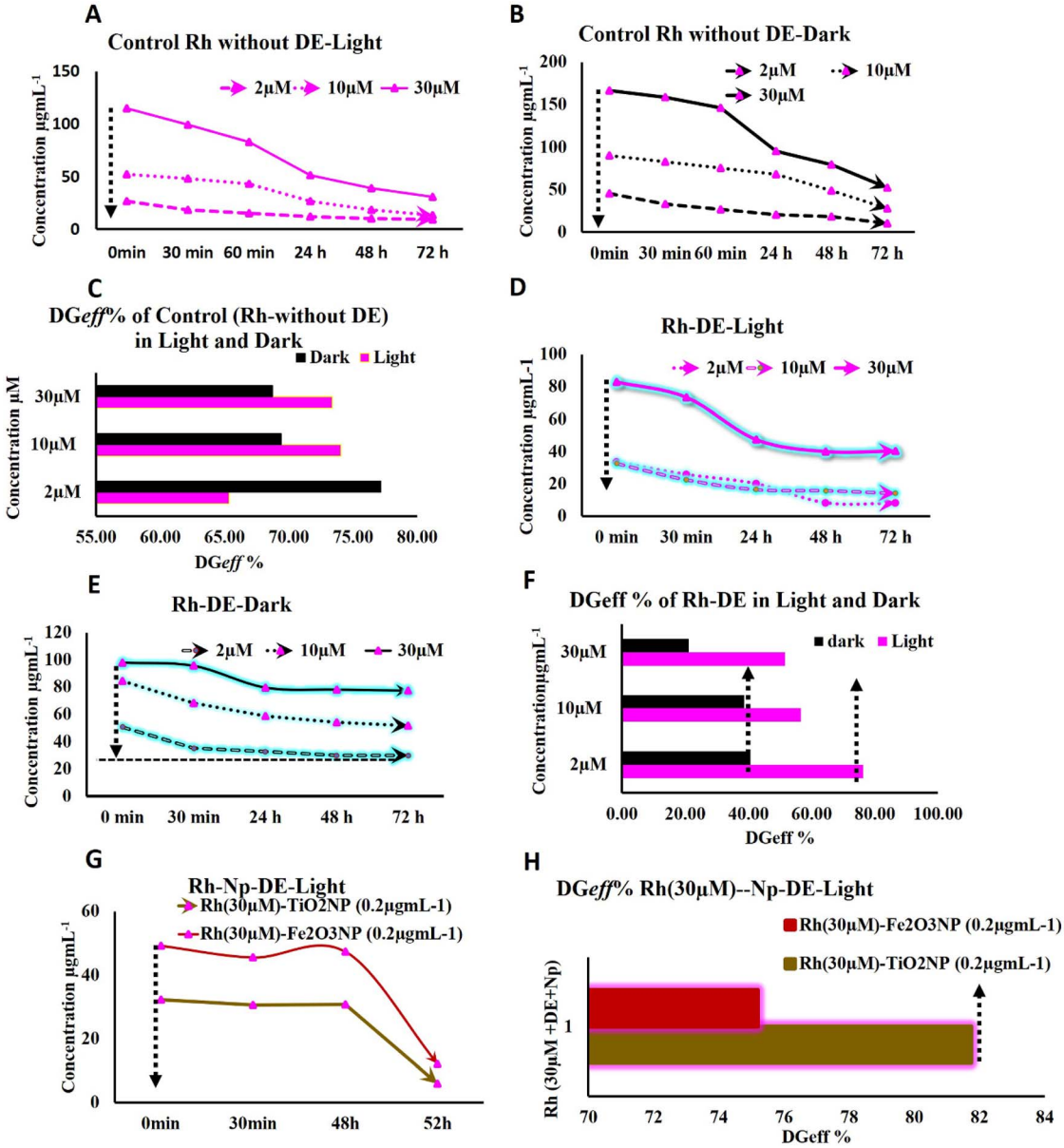

Fig. 4 Time-dependent (A) concentration of the control Rh sample without DE under light condition; (B) control Rh sample without DE under dark condition; (C) DG_{eff} of control Rh without DE under light and dark conditions; (D) Rh with DE under light condition; (E) concentration of Rh with DE under dark condition; (F) DG_{eff} of Rh and DE under light and dark conditions; (G) concentration of Rh (30 µM) with DE and nanoparticles (TiO_2 and Fe_3O_4) and (H) DG_{eff} of the highest Rh dye concentration in the presence of nanoparticles (TiO_2 and Fe_3O_4).

elemental analysis of NP(s) was characterised individually *via* EDX. ESI Fig. S4A and B† show the EDX plot for elemental analysis, confirming the presence of TiO_2 and Fe_3O_4, respectively. Further, both NP(s) were characterised for their characteristic crystal structures. ESI Fig. S4C† shows spectrum A (Sample A = TiO_2 on graphite felt) with titanium (Ti) present at 2.32 wt%, indicating the presence of titanium-based materials such as TiO_2 (titanium dioxide). Similarly, spectrum B (Sample B = Fe_3O_4 on graphite felt), in this iron (Fe) is present at 8.01 wt%, which suggests the presence of an iron-based material like Fe_3O_4 (magnetite) as the said NP(s) were already purchased. Both samples have a high carbon content (~75%), indicating that they are likely deposited on a graphite felt, with oxygen present in both samples, confirming the formation of oxides (TiO_2 in the A spectrum and Fe_3O_4 in the B spectrum).

The cathode had BG-11 media with microalgae coded as DNM_X, which was identified as *Asterarcys* sp. GA4 using primers 32F: TTGGATTCAAAGCTGGTGTT 634R: GAAACGG TCTCTCCAACGCAT based on nucleotide homology and phylogenetic analysis, as shown in ESI Fig. S5.† The evolutionary history was inferred by using the maximum likelihood method based on the Kimura 2-parameter model.[73] The bootstrap consensus tree inferred from 1000 replicates is taken to represent the evolutionary history of the taxa analysed. Branches

corresponding to partitions reproduced in less than 50% bootstrap replicates are collapsed. The percentages of replicate trees in which the associated taxa clustered together in the bootstrap test (1000 replicates) are shown next to the branches. Initial tree(s) for the heuristic search were obtained automatically by applying the Neighbour-Joining tree and BioNJ algorithms to a matrix of pairwise distances estimated using the maximum composite likelihood (MCL) approach, and then selecting the topology with a superior log likelihood value. The analysis involved 11 nucleotide sequences. The codon positions included were 1^{st} + 2^{nd} + 3^{rd} + noncoding. All positions containing gaps and missing data were eliminated. There were a total of 1434 positions in the final dataset. Evolutionary analyses were performed in MEGA X.

All the PMA-MFCs having an equal concentration of DE (100 g) and respective dyes (30 μM) (CBB, BG, and RH) and their respective NP(s) which acted as better nano catalysts in test tubes, were functionalized with DE on the graphite felt of anodes of each of the three PMA-MFCs and were run for 33 days with each cycle comprising 3 days. All the PMA-MFC's 1–3 reactors with microalgae *Asterarcys* sp. GA4 at the cathode and diatomite nanocomposites coated on its graphite felt at the anode rich in dye-simulated SWW showed enhanced DG_{eff} than their respective dye DE nanocomposites in test tubes under light and dark conditions.

It was seen that PMA-MFC reactor 1 with CBB (30 μM) dye–DE–Fe_3O_4 nanocomposites in anode containing SWW kept under total dark conditions generated electrons and underwent nanocatalytic and organic degradation generating electrons and protons, transitioning dye molecules into its lower forms of chemical moieties. The protons are transferred to the cathode *via* a proton exchange membrane, which combines with oxygen released during photosynthesis by microalgae and gets converted to water. Such photosynthesis-assisted microalgal microbial fuel cell (PMA-MFC) generated a total current density of 168.18 mA m^{-2} and maximum power density (PD_{max}) of 19.63 mW m^{-2}, on an average, for PMA-MFC-1 enriched with CBB–DE–Fe_3O_4 nanocomposites. The COD of PMA-MFC-1 was 55.71%, with a coulombic efficiency (CE%) of 6.66%, while the NER was 0.046 kW h m^{-3} (Fig. 5A). Fe NP(s) can improve the performance of PMA-MFC as an electron shuttle carrier.[74] Further Fe_3O_4 can stimulate the metabolism of electroactive microbes by acting as an electron sink or source, thus promoting their growth and electricity generation.

Similarly, PMA-MFC-2 rich in BG 30 μM dye–DE–TiO_2 nanocomposites at the anode with *Asterarcys* sp. GA4 at the cathode showed a total current density of 127.27 mA m^{-2} and a PD_{max} of 20.58 mW m^{-2}. The COD of PMA-MFC-2 was 57.55%, CE was 6.96% and NER was 0.057 kW h m^{-3} (Fig. 5B). PMA-MFC-1 and 2 had nearly the same maximum polarization

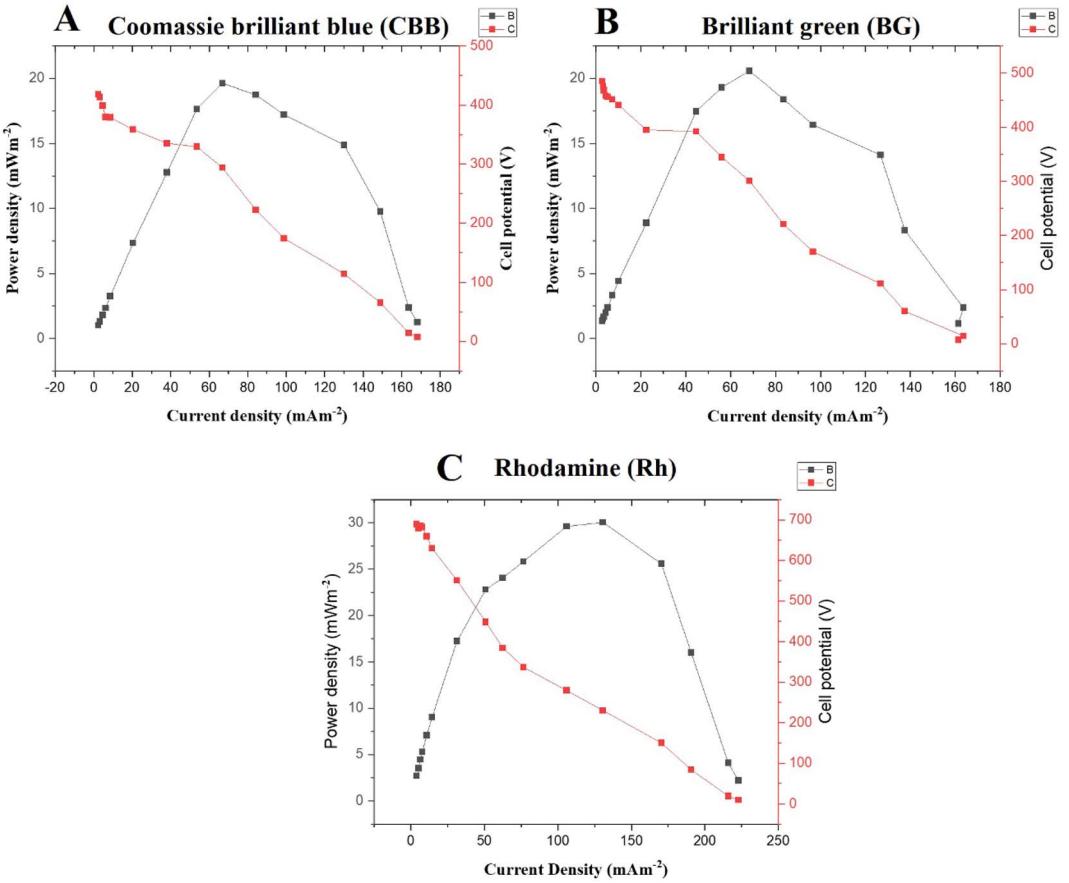

Fig. 5 Comparison of the polarization curve for PMA-MFC1-3 enriched with diatomite: (A) PMA-MFC 1 (diatomite–Coomassie brilliant blue–Fe_3O_4); (B) PMA-MFC 2 (diatomite–brilliant green–TiO_2) and (C) PMA-MFC 3 (diatomite–rhodamine–TiO_2).

density and COD. Microalgae at the cathode in PMA-MFC 1–3 play the role of oxygen producers while simultaneously producing their byproducts and biomass, which is an additional benefit of using such hybridized MFC set ups.

PMA-MFC-3, where the Rh dye at 30 μM DE–TiO_2 NP was used, showed maximum polarization density and COD. A total current density of 222.75 mA m^{-2} and a PD_{max} of 30.06 mW m^{-2} were observed in PMA-MFC-3 (Fig. 5C). The COD of PMA-MFC-3 was 61.36%, CE was 8.92% and NER was 0.046 kW h m^{-3}. The volt ampere curves of these PMA-MFCs 1, 2 and 3 showed a drop in voltage upon increase in the current with PMA-MFC-3, showing the lowest voltage drop (7.221 mV) and an increase in current (1.44 mA) (ESI Fig. S6A–C†).

PMA-MFC reactor 1 (CBB–Fe_3O_4), 2 (BG-TiO_2) and 3 (Rh–TiO_2) in darkness with dye (30 μM)–DE–NP(s) underwent biochemical and nanocatalytic oxidation and showed DG_{eff} values of 72.31%, 65.71% and 88.23%, respectively (ESI Fig. S7A and B†). On the offset, DG_{eff} for dye and DE without NP(s) in test tube kept in dark *i.e.*, CBB (30 μM)–DE, BG (30 μM)–DE and Rh (30 μM)–DE was 49.58%,; 22.82% and 21.4%, respectively, where only biochemical oxidation is taking place. This shows that nanocatalytic oxidation of dye–DE-nanocomposites at the anode in darkness in PMA-MFC is stronger than the dye functionalized with DE under dark conditions. Among, PMA-MFC better degradation of dye in anode simulated as dye rich SWW, under dark conditions was shown by PMA-MFC-3 with Rh

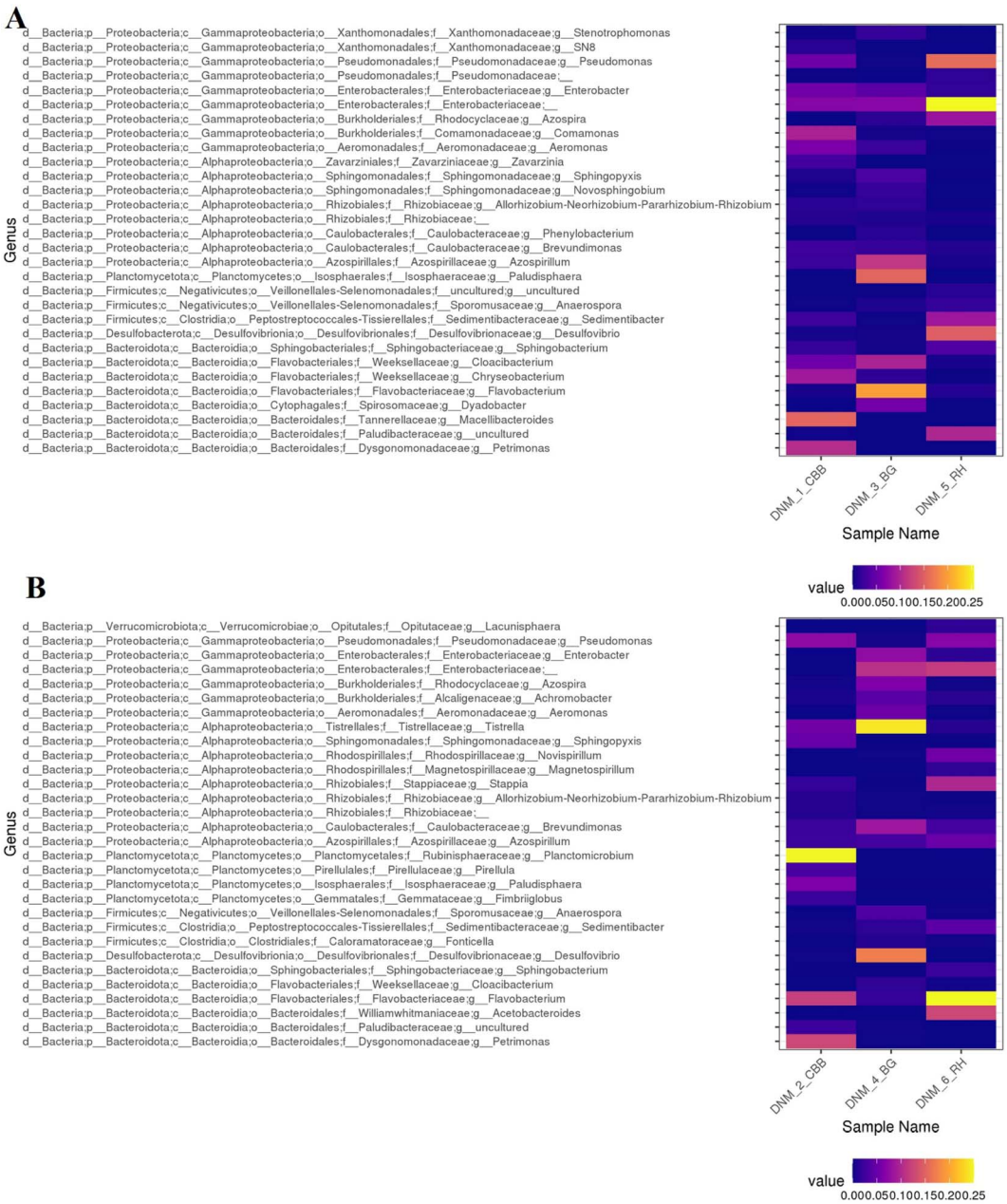

Fig. 6 Heat map of metagenomics data generated on the (A) initial and (B) final days at the anode section of PMA-MFC reactors 1–3 containing diatomite–Coomassie brilliant blue, brilliant green and rhodamine and nanoparticles on the initial and final days, respectively.

dye (88.23%) as seen in ESI Fig S7A and B†. The overall efficiency of PMA-MFC is also dependent upon the microbiota of wastewater at the anode during the initial and final days of its operation.[75] The DG_{eff} value of PMA-MFC is less than the individual photo-nanocatalysis for CBB (30 μM)–DE–Fe_3O_4, BG (30 μM)–DE–TiO_2 and Rh (30 μM)–DE–TiO_2, which was 84.46%, 96.10% and 81.74%, respectively. Photocatalysis is always better than catalysis in darkness, but PMA-MFC has yielded multiple value-added products such as bioelectricity, biomass, lipids and remediation of wastewater performing reasonably good even in darkness.

The purpose of analyzing three PMA-MFCs was to check which PMA-MFC supports the highest removal of dyes and multiple bioproduct production to make the overall process of remediation economic and efficient. Since all three PMA-MFCs had 30 μM of dye concentration as the threshold limit, which was tested in test tubes, it is essential to check other parameters too. The microbial consortium, which may be responsible for the organic degradation of dyes under dark conditions at the anode with microalgae at the cathode, is a very important factor to analyze.

3.4 Metagenomics of microbes in synthetic wastewater at the anode

The wastewater on the initial and final days of PMA-MFCs run in all three PMA-MFCs *i.e.* 1, 2 and 3, was taken for MID, and hence, extracted DNA was amplified using primers V3V4 forward and reverse, as observed in the PCR gel pictures, showing amplification at 460 bp present in PMA-MFCs 1, 2 and 3 on the initial and final days (ESI Table 2 and Fig. S8†). The MID analysis of the amplicon for PMA-MFC-1, PMA-MFC-2 and PMA-MFC-3 showed that different dyes affect the microbial diversity at the anode in a PMA-MFC. In PMA-MFCs 1 and 2 with CBB and BG dyes, the microbial diversity decreased on the final day of polarization cycle (Fig. 6 and S9†). However, PMA-MFC-3 with Rh dye and DE–Fe_3O_4 nanocomposite showed stable maintenance of existing microbial diversity, thus indicating its higher PD_{max} (30.06 mW m^{-2}) compared to PMA-MFCs 1 and 2 (~20 mW m^{-2}). In the present study, Proteobacteria, Bacteroidetes and Firmicutes remained dominant in PMA-MFCs 1 to 3 on the initial and final days of polarization cycle. The Venn diagram of all the three PMA-MFCs showed the shared species diversity among different sets on their first and final days of polarization (ESI Fig. S10†). The anode had different microbes

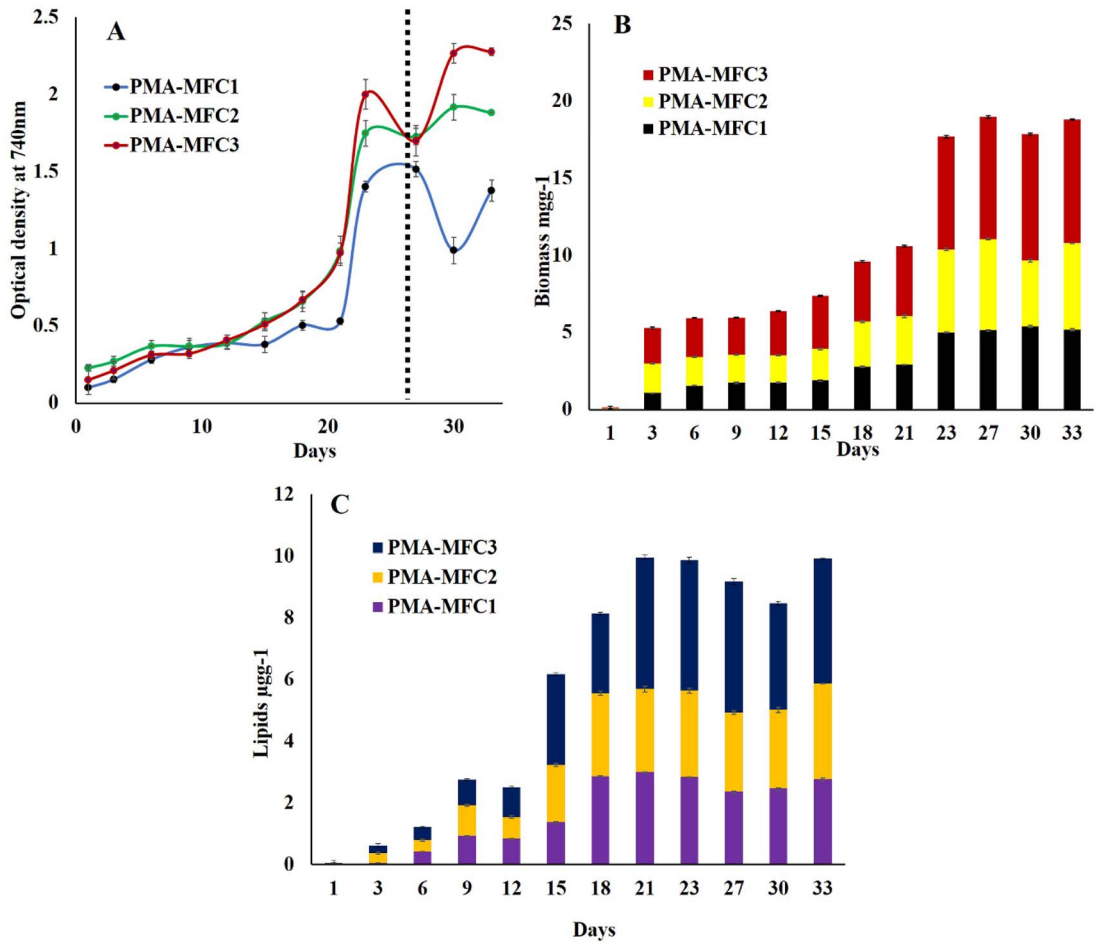

Fig. 7 Microalgae (*Asterarcys* sp.GA4) at the cathode for 40 days and measuring its (A) cell density, (B) biomass and (C) lipid yield on different days at the cathode of PMA-MFC 1–3.

changing their percentage population on the first and final days of the run of microbial fuel cells showing the dominance of Proteobacteria on the first day and Planctomycetes on the final day. PMA-MFC-2 with BG–DE dye showed Proteobacteria on both initial and final days and PMA-MFC-3 with Rh–DE nanocomposites showed dominance of Sphingobacteria and Proteobacteria. PMA-MFC-1 enriched with CBB at the anode had 25 out of 126 species in common, PMA-MFC-2 had 20 among 98 species in common and PMA-MFC-3 had 16 among 96 species in common present on the first and final days of polarization cycles.

3.5 Biochemical analysis of microalgae at the cathode

The microalgae *Asterarcys* sp. GA4 at the cathode of PMA-MFC showed maximum growth in terms of optical density on the 23rd day in all PMA-MFCs and was highest in PMA-MFC-1 (1.40) followed by PMA-MFC-2 (1.74) and PMA-MFC-3 (1.99) at 740 nm (Fig. 7A). The biomass of *Asterarcys* sp. GA4 was highest on the 30th day in PMA-MFC-3 (8.19 μg g^{-1}), followed by PMA-MFC-1(5.38 μg g^{-1}) and PMA-MFC-2 (4.28 μg g^{-1}) (Fig. 7B). The lipid from this microalga at the cathode was, however, highest in PMA-MFC-3 on the 21st day (4.278 μg g^{-1}), followed by 3.09 μg g^{-1} on the 33rd day in PMA-MFC-2 and 2.99 μg g^{-1} on the 21st day in PMA-MFC-1. Biomass of microalgae at cathode was, however, 2.769 μg g^{-1}, 3.09 μg g^{-1} and 4.054 μg g^{-1} on the 33rd day in PMA-MFCs 1, 2 and 3 with CBB, BG and Rh–DE-nanocomposite dyes at the anode respectively (Fig. 7C). The microalgal cell growth, biomass and lipids although showed higher shift for PMA-MFC 3, followed by PMA-MFC-2 and PMA-MFC-1 throughout its growth pattern. This is coherent with the high PD_{max} of PMA-MFC 3 followed by PMA-MFCs 2 and PMA-MFC-1. Many studies have demonstrated the use of microalgae at the cathode in a PMA-MFC, showing the production of lipids, biomass and other value-added products besides producing bioelectricity and remediating wastewater.[28,76,77]

The above study shows that PMA-MFC 3 with rhodamine dye and diatomite as the adsorbent and TiO_2 as the NP catalyst proved to be the most efficient microbial fuel cell in terms of remediating dye-rich wastewater. The overall efficiency has further confirmed PMA-MFC-3 as best in comparison with otherwise well-performed PMA-MFC-1 and PMA-MFC-2. A table of comparison evaluating the different parameters performed and analyzed at both chambers of all the three PMA-MFCs is seen in ESI Table S3.† ESI Table S4† shows the comparison of the present study with the previous studies, proving the present study's significant output in terms of dye degradation, bioelectricity production and value-added products in a PMA-MFC.

4 Conclusions

Dye removal is a very important need of the growing industrialization. In the current study, a comparison of three different ionic dyes, namely Coomassie brilliant blue, brilliant green and rhodamine, for their adsorption and degradation ability was carried out. All the three textile dyes followed the pseudo-second-order kinetics successfully, describing the adsorption process. Among these three, the dye–diatomite–TiO_2 nanocomposite has yielded better photocatalytic degradation efficiency. Further, the degradation efficiency of these dyes is economic in a photosynthetic microalgae-assisted microbial fuel cell. Among the different dyes tested in different fuel cells with the diatomite–Fe_3O_4 nanocomposite at the anode, with rhodamine dye has yielded the highest PD_{max}. The PD_{max} of PMA-MFC-1 and PMA-MFC-2 was less than that of PMA-MFC-3 but effective when observed individually with *Asterarcys* sp.GA4 microalgae. The high electrogenicity in PMA-MFC-3 is also associated with microbial population comprising Sphingobacteria and Proteobacteria identified by MID. Lipid production in PMMFC-1 (CBB), 2 (BG) and 3 (Rh) on the 33rd day of PMA-MFC, respectively, was in coherence with the growth pattern and efficiency of the fuel cell. PMA-MFC-3 yielded the highest lipid productivity on the 21st day. Future studies may need to focus on the degradation potential of these nanocomposites for other industrial dyes and pollutants. Indeed, the investigation of multi-dye systems or wastewater containing a mix of dyes could have impact on real-world applications.

Data availability

The data supporting this article have been uploaded as part of the ESI.†

Authors contribution

AR; VS: experimentation, data curation, and writing original draft; AA: data curation and analysis, GS; RK; AKS; H: review and editing; VV: supervision, conceptualization, writing original draft, funding, review, and editing.

Conflicts of interest

There are no conflicts to declare.

Acknowledgements

AR is thankful to Maharishi Markandeshwar Deemed University Haryana, India, VS is thankful to CEFIPRA Indo French Project for project fellowship, AA is thankful to CEFIPRA Indo French Project for senior research fellowship, GS is thankful to UGC for junior research fellowship, and VV is thankful to CEFIPRA Indo French Project No. PPMB 7133/2020 for financial support.

References

1 T. Akter, A. T. Protity, M. Shaha, M. Al Mamun and A. Hashem, in *Nanohybrid Materials for Treatment of Textiles Dyes*, Springer, 2023, pp. 401–431.
2 R. Kaur, S. Wani, A. Singh and K. Lal, Wastewater production, treatment and use in India, In *National Report presented at the 2nd regional workshop on Safe Use of Wastewater in Agriculture*, 2012, pp. 1–13.

3 A. B. Isaev, N. S. Shabanov, A. G. Magomedova, P. Nidheesh and M. A. Oturan, *Environ. Chem. Lett.*, 2023, **21**, 2863–2911.
4 G. Moussavi and M. Mahmoudi, *J. Hazard. Mater.*, 2009, **168**, 806–812.
5 R. Khanum, R. S. Ali, H. Rangaswamy, S. S. Kumar, A. Prashantha and A. Jagadisha, *Results Chem.*, 2023, **5**, 100890.
6 T. Islam, M. R. Repon, T. Islam, Z. Sarwar and M. M. Rahman, *Environ. Sci. Pollut. Res.*, 2023, **30**, 9207–9242.
7 R. Al-Tohamy, S. S. Ali, F. Li, K. M. Okasha, Y. A.-G. Mahmoud, T. Elsamahy, H. Jiao, Y. Fu and J. Sun, *Ecotoxicol. Environ. Saf.*, 2022, **231**, 113160.
8 N. Sheraz, A. Shah, A. Haleem and F. J. Iftikhar, *RSC Adv.*, 2024, **14**, 11284–11310.
9 Y. Fei and Y. H. Hu, *J. Mater. Chem. A*, 2022, **10**, 1047–1085.
10 M. J. Khan, A. Rai, A. Ahirwar, V. Sirotiya, M. Mourya, S. Mishra, B. Schoefs, J. Marchand, S. K. Bhatia and S. Varjani, *Bioengineered*, 2021, **12**, 9531–9549.
11 M. M. Ghobara, M. M. Ghobara, M. M. Ghobara and A. Mohamed, *Diatoms: Fundamentals and Applications*, 2019, pp. 471–509.
12 R. Patrick, *The Biology of Diatoms*, 1977, vol. 13, pp. 284–332.
13 V. Kumar, M. Kashyap, S. Gautam, P. Shukla, K. B. Joshi and V. Vinayak, *J. Biosci.*, 2018, **43**, 717–729.
14 M. J. Khan, D. Mathys and V. Vinayak, *Diatom Microscopy*, 2022, pp. 179–219.
15 M. Hildebrand, E. York, J. I. Kelz, A. K. Davis, L. G. Frigeri, D. P. Allison and M. J. Doktycz, *J. Mater. Res.*, 2006, **21**, 2689–2698.
16 D. Losic, G. Rosengarten, J. G. Mitchell and N. H. Voelcker, *J. Nanosci. Nanotechnol.*, 2006, **6**, 982–989.
17 T. T. Rahman, T. Jiang, C. Zhang, Y. Rao, R. C. Sims and L. Hou, *Crit. Rev. Environ. Sci. Technol.*, 2024, **54**, 557–580.
18 V. Vinayak, K. B. Joshi, R. Gordon and B. Schoefs, Nanoengineering of diatom surfaces for emerging applications, *Nanoscience & Nanotechnology Series*, 2017, pp. 55–78.
19 G. Sriram, M. P. Bhat, M. Kigga, U. Uthappa, H.-Y. Jung, T. Kumeria and M. D. Kurkuri, *Mater. Chem. Phys.*, 2019, **235**, 121738.
20 V. Hegde, U. Uthappa, S. S. Han, H.-Y. Jung, T. Altalhi and M. D. Kurkuri, *Mater. Today Commun.*, 2022, **32**, 103887.
21 B. E. Logan, B. Hamelers, R. Rozendal, U. Schröder, J. Keller, S. Freguia, P. Aelterman, W. Verstraete and K. Rabaey, *Environ. Sci. Technol.*, 2006, **40**, 5181–5192.
22 B. Logan, In *Microbial fuel cells*, John Wiely & Sons Inc, 2008.
23 M. J. Khan, N. Singh, S. Mishra, A. Ahirwar, F. Bast, S. Varjani, B. Schoefs, J. Marchand, K. Rajendran and J. R. Banu, *Chemosphere*, 2022, **288**, 132589.
24 J. Greenman, I. Gajda and I. Ieropoulos, *Sustainable Energy Fuels*, 2019, **3**, 2546–2560.
25 A. Ahirwar, S. Das, S. Das, Y.-H. Yang, S. K. Bhatia, V. Vinayak and M. M. Ghangrekar, *Algal Res.*, 2023, **70**, 102973.
26 M. J. Khan, V. J. Suryavanshi, K. B. Joshi, P. Gangadharan and V. Vinayak, in *Handbook of Algal Biofuels*, Elsevier, 2022, pp. 363–384.
27 M. Shukla and S. Kumar, *Renewable Sustainable Energy Rev.*, 2018, **82**, 402–414.
28 S. Arun, A. Sinharoy, K. Pakshirajan and P. N. Lens, *Renewable Sustainable Energy Rev.*, 2020, **132**, 110041.
29 S. Gupta, M. Kashyap, V. Kumar, P. Jain, V. Vinayak and K. B. Joshi, *J. Mol. Liq.*, 2018, **249**, 600–608.
30 Y. Nam, J. H. Lim, K. C. Ko and J. Y. Lee, *J. Mater. Chem. A*, 2019, **7**, 13833–13859.
31 D. Chen, Y. Cheng, N. Zhou, P. Chen, Y. Wang, K. Li, S. Huo, P. Cheng, P. Peng and R. Zhang, *J. Cleaner Prod.*, 2020, **268**, 121725.
32 R. Taghavi, S. Rostamnia, M. Farajzadeh, H. Karimi-Maleh, J. Wang, D. Kim, H. W. Jang, R. Luque, R. S. Varma and M. Shokouhimehr, *Inorg. Chem.*, 2022, **61**, 15747–15783.
33 N. Thakur, N. Thakur, A. Kumar, V. K. Thakur, S. Kalia, V. Arya, A. Kumar, S. Kumar and G. Z. Kyzas, *Sci. Total Environ.*, 2024, 169815.
34 I. Das, S. Das, R. Dixit and M. Ghangrekar, *Ionics*, 2020, **26**, 3061–3072.
35 S. Das, A. Mishra and M. Ghangrekar, *Chem. Phys. Lett.*, 2020, **759**, 137986.
36 S. Das and M. Ghangrekar, *Environ. Technol.*, 2020, **41**, 2546–2553.
37 J. L. Sanz and T. Köchling, *Process Biochem.*, 2007, **42**, 119–133.
38 A. Behle, *Recipe for standard BG-11 media*, 2019.
39 M. J. Khan, S. Das, V. Vinayak, D. Pant and M. Ghangrekar, *Chemosphere*, 2022, **291**, 132841.
40 L. Xiao, Z. Ge, P. Kelly, F. Zhang and Z. He, *Bioresour. Technol.*, 2014, **157**, 77–83.
41 K. Obileke, H. Onyeaka, E. L. Meyer and N. Nwokolo, *Electrochem. Commun.*, 2021, **125**, 107003.
42 B. E. Logan, *Nat. Rev. Microbiol.*, 2009, **7**, 375–381.
43 S. Ghosh and A. P. Das, *Frontiers in soil and environmental microbiology*, 2020, 247–254.
44 L. Karstens, N. Y. Siddiqui, T. Zaza, A. Barstad, C. L. Amundsen and T. A. Sysoeva, *Sci. Rep.*, 2021, **11**, 6186.
45 K. K. Yadav, Y. Nimonkar, B. J. Poddar, L. Kovale, I. Sagar, Y. Shouche, H. J. Purohit, A. A. Khardenavis, S. J. Green and O. Prakash, *Microbiol. Spectrum*, 2022, **10**, e00007–e00022.
46 N. A. Stover and A. R. Cavalcanti, *Curr. Protoc. Essent. Lab. Tech*, 2017, **14**, 111111–111134.
47 S. Kumar, G. Stecher, M. Li, C. Knyaz and K. Tamura, *Mol. Biol. Evol.*, 2018, **35**, 1547–1549.
48 M. J. Khan, N. Bawra, A. Verma, V. Kumar, A. Pugazhendhi, K. B. Joshi and V. Vinayak, *Bioresour. Technol.*, 2021, **319**, 124129.
49 S. Chowdhury and P. Saha, *Desalin. Water Treat.*, 2011, **30**, 229–236.
50 S. Devi and S. Tyagi, *RSC Adv.*, 2022, **12**, 34951–34961.
51 M. Pirilä, M. Saouabe, S. Ojala, B. Rathnayake, F. Drault, A. Valtanen, M. Huuhtanen, R. Brahmi and R. L. Keiski, *Top. Catal.*, 2015, **58**, 1085–1099.
52 M. Rauf and S. S. Ashraf, *Chem. Eng. J.*, 2009, **151**, 10–18.
53 W. Zhu and A. R. Kamali, *J. Water Process Eng.*, 2023, **53**, 103903.

54 B. M. Thamer, A. Aldalbahi, M. Moydeen, H. El-Hamshary, A. M. Al-Enizi and M. H. El-Newehy, *Mater. Chem. Phys.*, 2019, **234**, 133–145.
55 N. Liu, Y. Wu and H. Sha, *Sep. Sci. Technol.*, 2020, **55**, 234–246.
56 S. Dhananasekaran, R. Palanivel and S. Pappu, *J. Adv. Res.*, 2016, **7**, 113–124.
57 M. Sun, J. Ma, M. Zhang, Y. Xiao, Y. Zhu and S. Zhang, *Mater. Chem. Phys.*, 2020, **241**, 122450.
58 B. K. Nandi, A. Goswami and M. K. Purkait, *J. Hazard. Mater.*, 2009, **161**, 387–395.
59 V. S. Mane, I. D. Mall and V. C. Srivastava, *J. Environ. Manage.*, 2007, **84**, 390–400.
60 V. S. Mane, I. D. Mall and V. C. Srivastava, *Dyes Pigm.*, 2007, **73**, 269–278.
61 T. Calvete, E. C. Lima, N. F. Cardoso, S. L. Dias and E. S. Ribeiro, *Clean:Soil, Air, Water*, 2010, **38**, 521–532.
62 R. O. Gembo, S. Odisitse, T. A. Msagati and C. K. King'ondu, *Next Sustainability*, 2024, **4**, 100054.
63 M. S. U. Rehman, M. Munir, M. Ashfaq, N. Rashid, M. F. Nazar, M. Danish and J.-I. Han, *Chem. Eng. J.*, 2013, **228**, 54–62.
64 K. S. Baidya and U. Kumar, *S. Afr. J. Chem. Eng.*, 2021, **35**, 33–43.
65 N. Laskar and U. Kumar, *Int. J. Environ. Sci. Technol.*, 2019, **16**, 1649–1662.
66 M. Asadullah, M. Asaduzzaman, M. S. Kabir, M. G. Mostofa and T. Miyazawa, *J. Hazard. Mater.*, 2010, **174**, 437–443.
67 M. K. Khan, A. S. Abdulhameed, H. Alshahrani and S. Algburi, *Int. J. Biol. Macromol.*, 2024, **263**, 130465.
68 F. P. Andrew, T. R. Papo and P. A. Ajibade, *Environ. Adv.*, 2024, **17**, 100575.
69 S. Thakur, S. Singh and B. Pal, *J. Nanostruct. Chem.*, 2022, **12**, 207–221.
70 Y. Fang, M. Wu, Q. Zhang, F. Zhou, C. Deng, Y. Yan, H.-H. Shen, Y. Tang and Y. Wang, *Sep. Purif. Technol.*, 2022, **298**, 121611.
71 T. A. Saleh, M. Tuzen and A. Sarı, *Environ. Sci. Pollut. Res.*, 2021, **28**, 55655–55666.
72 S. K. Padmanabhan, S. Pal, E. U. Haq and A. Licciulli, *Appl. Catal., A*, 2014, **485**, 157–162.
73 E. B. Wong, N. Kamaruddin, M. Mokhtar, N. Yusof and R. F. R. Khairuddin, *J. Genet. Eng. Biotechnol.*, 2023, **21**, 104.
74 S. Zhao, S. Liu, T. Sumpradit, J. Zhou and J. Qu, *Int. J. Hydrogen Energy*, 2024, **63**, 163–172.
75 M. Li, M. Zhou, X. Tian, C. Tan, C. T. McDaniel, D. J. Hassett and T. Gu, *Biotechnol. Adv.*, 2018, **36**, 1316–1327.
76 J. K. Nayak and U. K. Ghosh, *Biomass Bioenergy*, 2019, **131**, 105415.
77 A. Khandelwal, A. Vijay, A. Dixit and M. Chhabra, *Bioresour. Technol.*, 2018, **247**, 520–527.